Check for updates

LIMNOLOGY and OCEANOGRAPHY

ASLO

Limnol. Oceanogr. 70, 2025, 360–376
© 2024 The Author(s). *Limnology and Oceanography* published by Wiley Periodicals LLC on behalf of Association for the Sciences of Limnology and Oceanography.
doi: 10.1002/lno.12765

Vertical nitrate flux fuels new production over summertime Northeast U.S. Shelf

Bofu Zheng [1*] **Weifeng (Gordon) Zhang** [2] **Rubao Ji** [1] **Rachel H. R. Stanley** [3] **E. Taylor Crockford** [1] **Diana N. Fontaine** [4] **Emily E. Peacock** [1] **Tatiana A. Rynearson** [4] **Heidi M. Sosik** [1]

[1]Biology Department, Woods Hole Oceanographic Institution, Woods Hole, Massachusetts, USA
[2]Applied Ocean Physics and Engineering Department, Woods Hole Oceanographic Institution, Woods Hole, Massachusetts, USA
[3]Chemistry Department, Wellesley College, Wellesley, Massachusetts, USA
[4]Graduate School of Oceanography, University of Rhode Island, Narragansett, Rhode Island, USA

Abstract

In aquatic ecosystems, allochthonous nutrient transport to the euphotic zone is an important process that fuels new production. Here, we use high-resolution physical and biogeochemical observations from five summers to estimate the mean vertical nitrate flux, and thus new production over the Northeast U.S. Shelf (NES). We find that the summertime nitrate field is primarily controlled by biological uptake and physical advection–diffusion processes, above and below the 1% light level depth, respectively. We estimate the vertical nitrate flux to be $8.2 \pm 5.3 \times 10^{-6}$ mmol N m^{-2} s^{-1} for the mid-shelf and $12.6 \pm 8.6 \times 10^{-6}$ mmol N m^{-2} s^{-1} for the outer shelf. Furthermore, we show that the new production to total primary production ratio (i.e., the f-ratio), consistently ranges between 10% and 15% under summer conditions on the NES. Two independent approaches—nitrate flux-based new production and O_2/Ar-based net community production—corroborate the robustness of the f-ratio estimation. Since ~ 85% of the total primary production is fueled by recycled nutrients over sufficiently broad spatial and temporal scales, less than 15% of the organic matter produced in summer is available for export from the NES euphotic zone. Our direct quantification of new production not only provides more precise details about key processes for NES food webs and ecosystem function, but also demonstrates the potential of this approach to be applied to other similar datasets to understand nutrient and carbon cycling in the global ocean.

Despite covering only ~ 8% of the surface area of the ocean, continental shelf regions support ~ 15–20% of primary production globally (Longhurst et al. 1995). This primary productivity not only plays a critical role in the cycling of essential biogeochemical elements (Fennel et al. 2006), but also provides enormous economic value of over billions of US dollars through commercial fishing (National Marine Fisheries Service 2021). Moreover, as a valuable component of the marine biosphere, the shelf region is home to many endangered high-trophic-level marine species, for example, Atlantic salmon (Gilbey et al. 2021), the North Atlantic right whale (Record et al. 2019), and the Steller sea lion (Jemison et al. 2018). Food and energy support for these higher trophic levels depends on complex planktonic food webs in the lower trophic levels that rely on the supply of nutrients for the photosynthetic production of organic matter.

As a temperate shelf, the Northeast U.S. Shelf (NES), spanning from Cape Hatteras in the south to the Gulf of Maine in the north, is one of the most biologically productive regions in the ocean (O'Reilly and Zetlin 1998; Sherman et al. 2002). Evidence points to inorganic nitrogen as the limiting macronutrient for primary production in the NES system (Sedwick et al. 2018; Zang et al. 2021). Quantification of the nitrate dynamics is important for understanding the structure as well

*Correspondence: bzheng@whoi.edu

Additional Supporting Information may be found in the online version of this article.

This is an open access article under the terms of the Creative Commons Attribution License, which permits use, distribution and reproduction in any medium, provided the original work is properly cited.

Author Contribution Statement: BZ: Conceptualization; Formal analysis; Investigation; Methodology; Writing—original draft preparation; Writing—review and editing. WZ: Conceptualization; Funding acquisition; Investigation; Methodology; Writing—review and editing. RJ: Conceptualization; Funding acquisition; Investigation; Methodology; Writing—review and editing. RHRS: Funding acquisition; Methodology; Writing—review and editing. ETC: Methodology; Writing—review and editing. DNF: Methodology; Writing—review and editing. EEP: Methodology; Writing—review and editing. TAR: Funding acquisition; Methodology; Writing—review and editing. HMS: Conceptualization; Funding acquisition; Investigation; Methodology; Writing—review and editing.

as the spatial and temporal evolution of food webs (Falkowski et al. 2003; Sigman and Hain 2012). Previous works have focused on nitrate uptake (e.g., Harrison et al. 1983), transport (e.g., Townsend et al. 2015), and cycling (e.g., Ketchum et al. 1958; Fennel et al. 2006; Hales et al. 2009). Nitrate concentration in the euphotic zone on the NES exhibits strong seasonality, characterized by a concentration of nearly 0 μM (below the detection limit of 0.04 μM) during summer, much higher concentration (over 5 μM) during winter, and intermediate concentration during spring and fall (Oliver et al. 2022). Nitrate from allochthonous pathways (including lateral transport, vertical supply, and atmospheric deposition) into the euphotic zone fuels new production (e.g., Dugdale and Goering 1967). This new production has been suggested to account for $\sim$ 10% to $\sim$ 40% of total primary production over the NES depending on geographic location and period of interest (e.g., Harrison et al. 1983; Townsend 1998; Franks and Chen 2001; Bisagni 2003). These previous studies quantified new production to total primary production ratios, that is, the f-ratio, with indirect approaches, typically through inference from incubation-based estimates of nitrate vs. nitrate + ammonium uptake rates (e.g., Dugdale and Goering 1967; Eppley and Peterson 1979).

Direct quantification of new nitrate flux (and associated new production) remains lacking for the NES region. This paucity of information not only limits our understanding of nitrate transport pathways, but also confounds the accurate projection of future climate impacts and feedbacks on the local ecosystem. This is because changes in new production have the potential to shift the regional CO_2 source-sink balance between the ocean and atmosphere. To date, it is the lack of long-term high spatial and temporal resolution nitrate concentration measurements that primarily limits our ability to characterize the nitrate flux and relevant nitrate dynamics in the NES.

The recently established Northeast U.S. Shelf Long-Term Ecological Research (NES-LTER) project offers an ideal opportunity to fill those knowledge gaps. Facilitated by a wide scope of physical, biological, and chemical measurements, the NES-LTER project aims to improve our understanding of the key processes of the NES ecosystem (e.g., Marrec et al. 2021; Zang et al. 2022; Honda et al. 2023; Stevens et al. 2023; Castillo Cieza et al. 2024). Here, we use nitrate measurements collected by a submersible ultraviolet nitrate analyzer (SUNA) mounted on a CTD rosette to characterize the nitrate profiles in an unprecedentedly high vertical resolution, with spatial coverage spanning across the inner continental shelf to upper continental slope on a multi-year basis. These nitrate profiles allow direct quantification of the upward nitrate flux into the euphotic zone over the NES during the summertime—a target season when biological productivity is high (Fennel et al. 2006). As the upward nitrate flux is the primary nitrate source to fuel new production in the sunlit surface layer, our SUNA-based approach provides a direct estimate of the f-ratio on the NES with an accuracy much higher than estimates from traditional indirect approaches.

Materials and methods

NES-LTER observations

NES-LTER survey cruises cover a cross-shelf transect spanning southward from Martha's Vineyard, MA, to just beyond the shelf break—a total distance of $\sim$ 150 km (Fig. 1), once a season since winter 2018. Along the transect, about 21 stations are routinely occupied and a suite of ship-based measurements are made, including (1) physical and biogeochemical variables, such as temperature, salinity, current velocity, nutrient concentration, and chlorophyll *a* concentration; (2) rate parameters, such as net primary production (NPP) rate, total primary production rate, net community production (NCP) rate, phytoplankton growth rate, and microzooplankton grazing rate; and (3) biological community composition, spanning bacterioplankton, phytoplankton, microzooplankton, mesozooplankton, and forage fish. Note that some parameters are only measured at the stations, or a

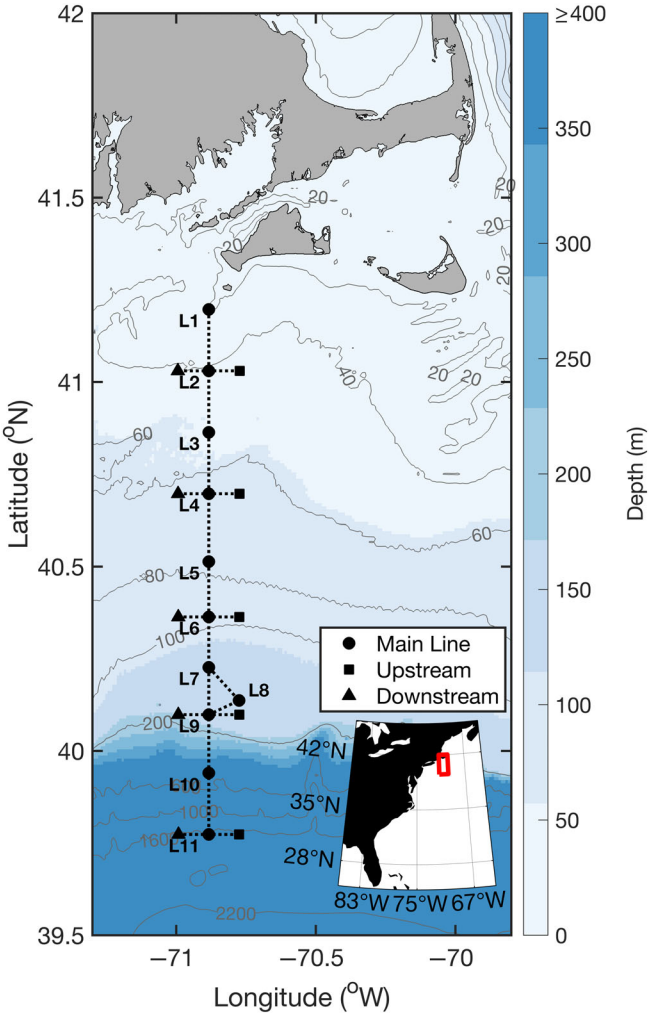

Fig. 1. Northeast U.S. Shelf Long-Term Ecological Research station map. The gray lines are bathymetry contours in meters. Note that L8 shifted westward to the main north–south line since the start of 2023.

19395590, 2025, 2, Downloaded from https://aslopubs.onlinelibrary.wiley.com/doi/10.1002/lno.12765 by Mbl Whoi Library, Wiley Online Library on [21/05/2025]. See the Terms and Conditions (https://onlinelibrary.wiley.com/terms-and-conditions) on Wiley Online Library for rules of use; OA articles are governed by the applicable Creative Commons License

subset of the stations, on the main north–south line. In this work, data from five recent summer cruises (2019–2023; Table 1) are used.

SUNA data quality control

SUNA-measured nitrate data were quality controlled by applying appropriate postprocessing algorithms to achieve adequate accuracy (representing how close a measurement is to the true value) and precision (representing how close measurements are to each other when measuring under the same condition). Zheng et al. (2024) documented the detailed quality control procedures that build upon the algorithms in Sakamoto et al. (2009, 2017) and Plant et al. (2023). We report the accuracy of quality-controlled SUNA nitrate data as the root mean square error referenced to discrete bottle data:

$$\text{Root mean square error} = \sqrt{\frac{1}{m}\sum_{i=1}^{m}(S_i - B_i)^2} \quad (1)$$

where m is the total number of discrete bottled samples, S is SUNA nitrate concentration, B is nitrate concentration of the discrete bottle samples that are analyzed at the Woods Hole Oceanographic Institution Nutrient Analytical Facility with a four-channel segmented flow AA3 HR Autoanalyzer, with an accuracy of 0.04 μM for nitrate + nitrite ($NO_3 + NO_2$), and i represents the index of the discrete samples. The final quality-controlled SUNA nitrate data has an accuracy of $\sim$0.6 μM (Table 1; Fig. 2) and a precision of $\sim$0.19 μM Zheng et al. (2024).

Obtaining mean nitrate profiles

To facilitate the characterization of the shape of the nitrate profile as well as the quantification of the vertical nitrate gradient, nitrate profiles collected from individual stations were averaged both spatially over the shelf region and temporally over multiple years. Specifically, we determined summertime mean nitrate profiles by first averaging individual nitrate profiles collected at each station during four summers (2020–2023) and then grouping the station averaged nitrate profiles into three different cross-shelf sections, namely, the inner shelf, mid-shelf, and outer shelf, respectively.

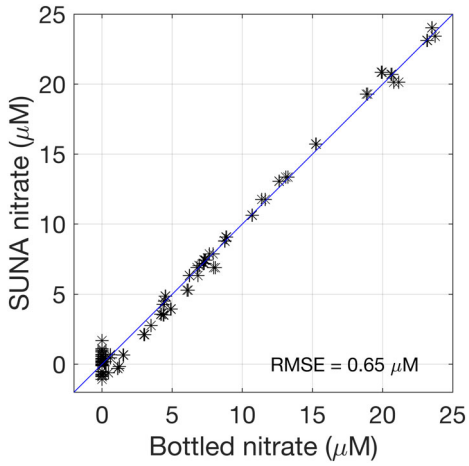

Fig. 2. Quality-controlled submersible ultraviolet nitrate analyzer (SUNA) nitrate data vs. discrete bottle nitrate data compiled from 12 SUNA profiles from the 2022 summer transect. The blue line represents the 1 : 1 ratio. *See* Zheng et al. (2024) for more statistics for all cruises. RMSE, root mean square error.

The NES is a well-known hotspot of internal waves, particularly high-frequency internal waves with significant vertical isopycnal displacements (Colosi et al. 2001). These isopycnal movements would induce vertical heaving of isonitrate surfaces, which complicates the averaging of individual nitrate profiles. Thus, we applied a depth-to-isopycnal coordinate conversion to minimize local temporal fluctuations in the nitrate profile, mainly due to passing internal waves (e.g., Zheng et al. 2023). The coordinate conversion was completed in three steps. First, we obtained mean depths of isopycnal layers. This mean isopycnal depth was estimated by averaging the depth of each density bin (the density interval was set as a uniform 0.01 kg m^{-3}) across all individual profiles collected at the same station over multiple years (Fig. 3b). Second, we obtained the mean nitrate concentration in each density bin. At each station, individual nitrate profiles were

Table 1. Five summer Northeast U.S. Shelf Long-Term Ecological Research cruises considered in this work.

Cruise name	Date of the cruise	Number of SUNA profiles	Root mean square error of the quality-controlled SUNA nitrate data (μM)	Notes
EN644	Aug 19–24, 2019	28	0.69	Unusual *Hemiaulus* bloom $\sim$ 40.4–41°N and noticeable Gulf Stream water intrusion south of $\sim$ 40.3°N
EN655	Jul 25–28, 2020	16	0.48	Generally typical summertime situation
EN668	Jul 16–21, 2021	22	0.58	Generally typical summertime situation
EN687	Jul 29–Aug 3, 2022	25	0.65	Generally typical summertime situation
EN706	Aug 7–12, 2023	24	0.78	Generally typical summertime situation

SUNA, submersible ultraviolet nitrate analyzer.

19395590, 2025, 2, Downloaded from https://aslopubs.onlinelibrary.wiley.com/doi/10.1002/lno.12765 by Mbl Whoi Library, Wiley Online Library on [21/05/2025]. See the Terms and Conditions (https://onlinelibrary.wiley.com/terms-and-conditions) on Wiley Online Library for rules of use; OA articles are governed by the applicable Creative Commons License

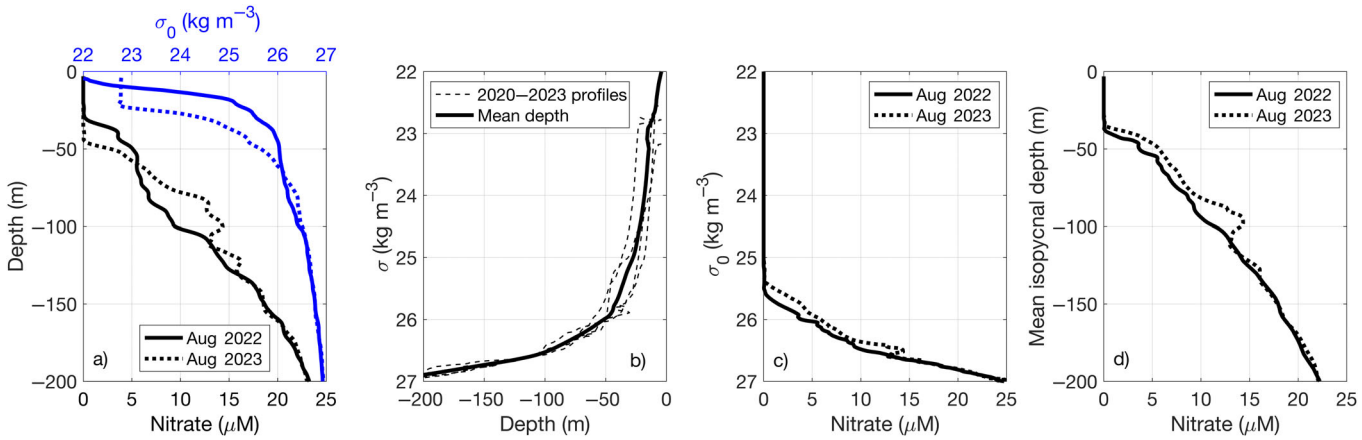

Fig. 3. Example profiles illustrating steps of the depth-to-isopycnal coordinate transformation. (**a**) Nitrate profiles (black) and corresponding density profiles (blue) in the original depth coordinate system as measured at station L10 in 2022 and 2023; (**b**) a mean density-depth profile (solid line) and all measured density-depth profiles (dashed lines) used to obtain the mean profile at L10; (**c**) nitrate profiles transformed to the density coordinate; (**d**) converted nitrate profiles as a function of mean isopycnal depth.

converted from the depth coordinate system into the isopycnal coordinate system by interpolating the quality-controlled SUNA nitrate (as a function of density) onto the uniformly gridded density bins (Fig. 3c). Subsequently, all the converted nitrate profiles located at the same station were averaged in the same density bin, which generated a station-mean nitrate profile. Finally, the station-mean nitrate profile is stored as a function of the mean depth of each density bin, which is obtained from the first step (Fig. 3d). This third step accounts for the squeezing and stretching of density layers (or in other words, change of stratification). To illustrate the depth-to-isopycnal coordinate transformation procedures, two profiles of nitrate and density collected at the same station are shown in Fig. 3, where the coordinate-transformed results show that isobaric nitrate differences (at $\sim$ 30–70 m, black and dotted line; Fig. 3a) can be largely minimized (Fig. 3d).

We divide the entire shelf area into three cross-shelf sections as determined by the mean salinity over the water column shallower than 100 m (Mountain 2003): inner shelf with salinity < 32.5 psu; mid-shelf with salinity between 32.5 and 33.5 psu; outer shelf with salinity > 33.5 psu. Following these criteria, each station-mean nitrate profile was assigned to a cross-shelf section. Note that within the same cross-shelf section, each station-mean nitrate profile was shifted vertically by aligning its nitracline (taken as the vertical position where nitrate concentration is 1 μM higher than the surface value) to the average depth of the nitracline of this section. This alignment accounts for the cross-shelf variation of the nitracline depth. Finally, the section-mean nitrate profile was obtained by taking the median value of all the aligned station-mean nitrate profiles within each 2-, 3-, and 5-m depth bin for the inner-, mid-, and outer-shelf sections, respectively. Note that the larger vertical bin size for the more offshore section is to allocate enough points for averaging in response to the fact that the depth difference between consecutive density layers is larger when stratification is lower for the deeper water.

Vertical diffusivity

Turbulent mixing can distribute dissolved tracers vertically in the ocean (Caldwell and Mourn 1995). Mixing strength can be parameterized by vertical diffusivity. Since we did not directly measure vertical diffusivity or other turbulent properties, we here apply a turbulence parameterization following the MacKinnon–Gregg method (MacKinnon and Gregg 2005) to quantify vertical diffusivity. The method is based on the assumption that, in a steady-state broadband internal wave field, turbulent energy dissipation rate is controlled by the interaction among internal waves (Henyey et al. 1986). Turbulent energy dissipation rate can thus be scaled as:

$$\varepsilon_{MG} = \varepsilon_0 \frac{S}{S_0} \frac{N}{N_0} \tag{2}$$

where ε_0 is a reference dissipation rate,

$$S = \sqrt{\left(\frac{du}{dz}\right)^2 + \left(\frac{dv}{dz}\right)^2} \tag{3}$$

is the vertical shear of horizontal velocities induced by low-frequency, low-mode internal waves, S_0 is a reference velocity shear,

$$N = \sqrt{\frac{g}{\rho_0}\frac{\partial \rho}{\partial z}} \tag{4}$$

is buoyancy frequency, representing vertical stratification, N_0 is a reference buoyancy frequency, u and v are eastward and northward velocities, respectively, z is depth, g is gravitational

19395590, 2025, 2, Downloaded from https://aslopubs.onlinelibrary.wiley.com/doi/10.1002/lno.12765 by Mbl Whoi Library, Wiley Online Library on [21/05/2025]. See the Terms and Conditions (https://onlinelibrary.wiley.com/terms-and-conditions) on Wiley Online Library for rules of use; OA articles are governed by the applicable Creative Commons License

acceleration, ρ is density, and $\rho_0 = 1024\,\mathrm{kg\,m^{-3}}$ is the reference density. Following MacKinnon and Gregg (2005), we choose $S_0 = N_0 = 3\,\mathrm{cycles\,h^{-1}}$, and $\varepsilon_0 = 1.1 \times 10^{-9}\,\mathrm{W\,kg^{-1}}$. Once ε is estimated, vertical diffusivity (k_v) can be calculated following the Osborn–Cox parameterization (Osborn 1980) under the assumption of a turbulent kinetic energy balance between production and dissipation. It gives:

$$k_v = \Gamma \frac{\varepsilon}{N^2} \tag{5}$$

where, Γ is the mixing efficiency, taken as 0.2 (Gregg et al. 2018). The applicability of the MacKinnon–Gregg method in quantifying turbulence has been verified in many locations, including the continental shelf south of New England (MacKinnon and Gregg 2005), the Baltic Sea (van der Lee and Umlauf 2011), and the Southern California Bight (Omand et al. 2012). Following this method, we utilized velocity measurements from the shipboard acoustic Doppler current profiler and stratification data from CTD casts to estimate vertical profiles of the vertical diffusivity. To increase velocity precision, we first averaged velocity data within a circle of 200-m radius centered on the location of each CTD cast. For each station, the velocity shear and stratification profiles were computed from Eqs. 3 and 4 and then averaged isobarically across all available profiles collected at the same station to obtain temporal mean profiles (Fig. 4a). The mean velocity shear and stratification profiles were subsequently fed into Eqs. 2 and 5 to obtain a mean diffusivity profile (Fig. 4b). The estimated mean diffusivity profile at each station is assigned to the three cross-shelf sections following the same salinity-based criteria as explained earlier.

Vertical nitrate flux estimation

We seek to quantify vertical nitrate flux and provide a direct estimate of the amount of nitrate being transported from the deeper part of the water column into the euphotic zone. From the nitrate and diffusivity profiles, the vertical diffusive nitrate flux (F_n) over the water column can be estimated with:

$$F_n = k_v \frac{\partial n}{\partial z} \tag{6}$$

O_2/Ar and triple oxygen isotope methods

Net community production was determined from measurements of O_2/Ar; oxygen is sensitive to photosynthesis and respiration and argon serves as an abiotic analog. O_2/Ar was measured every 30 s throughout each cruise from the ship's underway science seawater across the transect (intake depth = 5 m on the *R/V Endeavor*) using an equilibrator inlet mass spectrometer system (Cassar et al. 2009). More specifically, water from the underway system was pumped by a diaphragm pump and passed through a debubbler into a bucket. A gear pump was then used to pump water at a rate of 1100 mL $\mathrm{min^{-1}}$ from the bucket, through 25 and 100 μm filters, into an equilibrator membrane contractor cartridge (Liqui-Cel Extraflow 2.5 × 8 model G540). The gas from the water equilibrated with the headspace, was dried, and then transferred via a fused silica capillary into a Hiden quadrupole mass spectrometer (Hiden RGA Hal 7). The system was calibrated every 4–6 h by measuring the O_2/Ar ratio in air. Additionally, bottle samples (*see* details below) were collected from the underway multiple times per day, analyzed postcruise with an isotope ratio mass spectrometer, and used to further calibrate the equilibrator inlet mass spectrometer system data. NCP was calculated from the O_2/Ar ratios using solubility data of Garcia and Gordon (1992) and Hamme and Emerson (2004), the gas exchange parameterization of Stanley et al. (2009), and NCEP reanalysis winds (Kistler et al. 2001), exactly as described in Castillo Cieza et al. (2024).

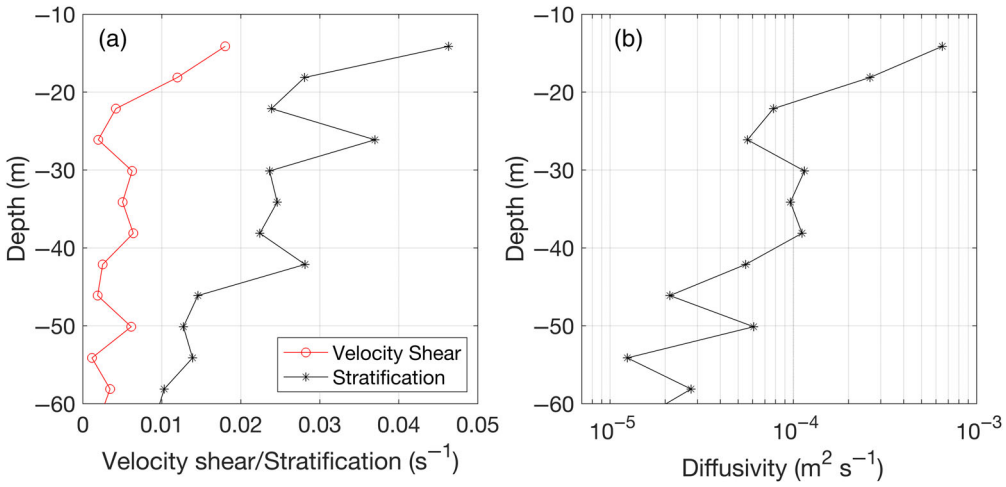

Fig. 4. Example vertical profiles of (**a**) velocity shear and stratification and (**b**) diffusivity computed from Eqs. 2–5. Note that the *x*-axis in (**b**) has a logarithmic scale.

19395590, 2025, 2, Downloaded from https://aslopubs.onlinelibrary.wiley.com/doi/10.1002/lno.12765 by Mbl Whoi Library, Wiley Online Library on [21/05/2025]. See the Terms and Conditions (https://onlinelibrary.wiley.com/terms-and-conditions) on Wiley Online Library for rules of use; OA articles are governed by the applicable Creative Commons License

Gross oxygen production, which is a measure very similar to gross primary production (GPP; Juranek and Quay 2013), was determined from triple oxygen isotope samples, collected from Niskins or the underway water into preevacuated 500-mL custom-made flasks poisoned with 100 μL of mercuric chloride. The bottles were filled to approximately 300 mL and the gas from the water equilibrated with the headspace. Once onshore, water was drained out of the bottles and the gasses were processed through a custom-made triple oxygen isotope line and analyzed with a 253 MAT isotope ratio mass spectrometer. For more details, *see* Castillo Cieza et al. 2024. Gross oxygen production was calculated from the ratios of $^{17}O/^{16}O$ and $^{18}O/^{16}O$ using the equations of Prokopenko et al. (2011). Additionally, bottle samples were used to determine that the O_2/Ar and triple oxygen isotope of the underway water were identical to that of the surface water as sampled by the Niskins from the CTD.

NPP estimation

Here we provide an overview of the ^{13}C method to quantify NPP, with more detailed descriptions of the method provided in Fontaine et al. (2025). Water from Niskin bottles was collected from 3 to 4 depths and prefiltered through 200-μm mesh into acid-washed 2-L polycarbonate bottles. Bottles were spiked with a solution of 99% $NaH^{13}CO_3$ (Cambridge Isotope Lab) for a final 10% enrichment of the dissolved inorganic carbon pool (the average enrichment was 10.8% ± 0.4%). Then bottles were placed in neutral density mesh bags with known light attenuation properties to simulate in situ light levels (ranging from 0.1% to 65% of the surface light intensity). Bottles were then incubated for ~ 24 h in deck-board incubators with flow-through seawater. Following the 24-h incubation in 2-L bottles, sample water was aliquoted (600 mL) and filtered under low vacuum (< 20 kPa) onto a precombusted Whatman GF/F filter (450°C; 6 h). Filters were stored at − 20°C until further analysis on shore. Discrete NPP rates (μgC L^{-1} d^{-1}) were quantified from the fraction of the isotopically heavy carbon incorporated into phytoplankton biomass using Eq. 7 (Hama et al. 1983):

$$\mathrm{NPP} = \frac{C \times (a_{\mathrm{is}} - a_{\mathrm{ns}})}{t \times (a_{\mathrm{ic}} - a_{\mathrm{ns}})} \times 1.025 \tag{7}$$

where C is the amount of particulate organic carbon at the end of the incubation (μgC L^{-1}), t is the incubation time (days), a_{is} is the atom % of ^{13}C in the incubated sample, a_{ic} is the atom % of ^{13}C in the total inorganic carbon pool, and a_{ns} is the atom % of ^{13}C in the natural abundance sample. We used an isotope discrimination factor of 1.025 following Hama et al. (1983). The NPP measurements are used to approximate the biological uptake rate of nitrate for waters below the euphotic zone.

Euphotic depth estimation

The euphotic depth (Z_{eu}), taken as the depth where the photosynthetically available radiation (PAR) is 1% of its surface value, was estimated from PAR profiles measured during the CTD-rosette casts, assuming PAR exponentially decreases with depth:

$$\mathrm{PAR}(z) = \mathrm{PAR}_0\, e^{-k(z)z} \tag{8}$$

where $\mathrm{PAR}(z)$ is the measured PAR profile, PAR_0 is surface PAR, and $k(z)$ is the depth-dependent diffuse attenuation coefficient. PAR_0 was estimated by first linear regressing $\log(\mathrm{PAR}(z))$ against depth within the surface 10 m and then exponentiating the y-intercept value, because z is zero (i.e., at the surface) there. Subsequently, Z_{eu} is obtained by locating the depth where $\mathrm{PAR}(z)$ is 1% of the calculated PAR_0. This approach relies directly on the measured PAR profile, and depth dependence of $k(z)$ (e.g., higher k within the subsurface chlorophyll maximum layer) is embedded in the calculation.

Mean cross-shore velocity

The Ocean Observatories Initiative Coastal Pioneer Array was a set of physical and biogeochemical moorings that was located at the shelf edge to the south of New England during 2014–2023 (Gawarkiewicz and Plueddemann 2020). Horizontal velocity data were collected at a few of the mooring sites by upward-looking acoustic Doppler current profilers at a temporal resolution ranging from 30 min to 1 h and a vertical resolution from 4 to 8 m (depending on the instrumentation type and configuration). Here, we obtain the mean cross-shore velocity by averaging the north–south velocity component isobarically over the summers of 2020–2022.

Results

The summertime section-mean nitrate profiles exhibit cross-shelf variations. The inner shelf nitrate is relatively uniform over the whole water column, with nitrate concentration close to zero from the surface to ~ 20 m depth, and increasing to ~ 0.5 μM near the bottom (Fig. 5a). The mid-shelf nitrate profile has two distinct layers (Fig. 5b). Specifically, a well-mixed surface layer is characterized by zero nitrate down to a depth of approximately 1% light intensity. In the layer below, nitrate concentration generally increases exponentially with depth, and a least-squares fit to the mean nitrate vertical profile gives: $n = 10.7 - 27e^{0.03z}$, where n is nitrate concentration in μM and z is depth in meters. In the outer-shelf section, the mean nitrate profile presents a three-layer structure, where the surface nitrate-depleted layer extends from the surface down to approximately the 1% light level depth, followed by a middle layer of nitrate exponentially increasing with depth to approximately 70 m, and then a deep layer where nitrate concentration linearly increases with depth (Fig. 5c). The mean profiles in the lower two layers can be represented as: $n = 9.9 - 36.2e^{0.035z}$, and $n = -0.13z - 1.99$, respectively, following least-squares fit procedures.

19395590, 2025, 2, Downloaded from https://aslopubs.onlinelibrary.wiley.com/doi/10.1002/lno.12765 by Mbl Whoi Library, Wiley Online Library on [21/05/2025]. See the Terms and Conditions (https://onlinelibrary.wiley.com/terms-and-conditions) on Wiley Online Library for rules of use; OA articles are governed by the applicable Creative Commons License

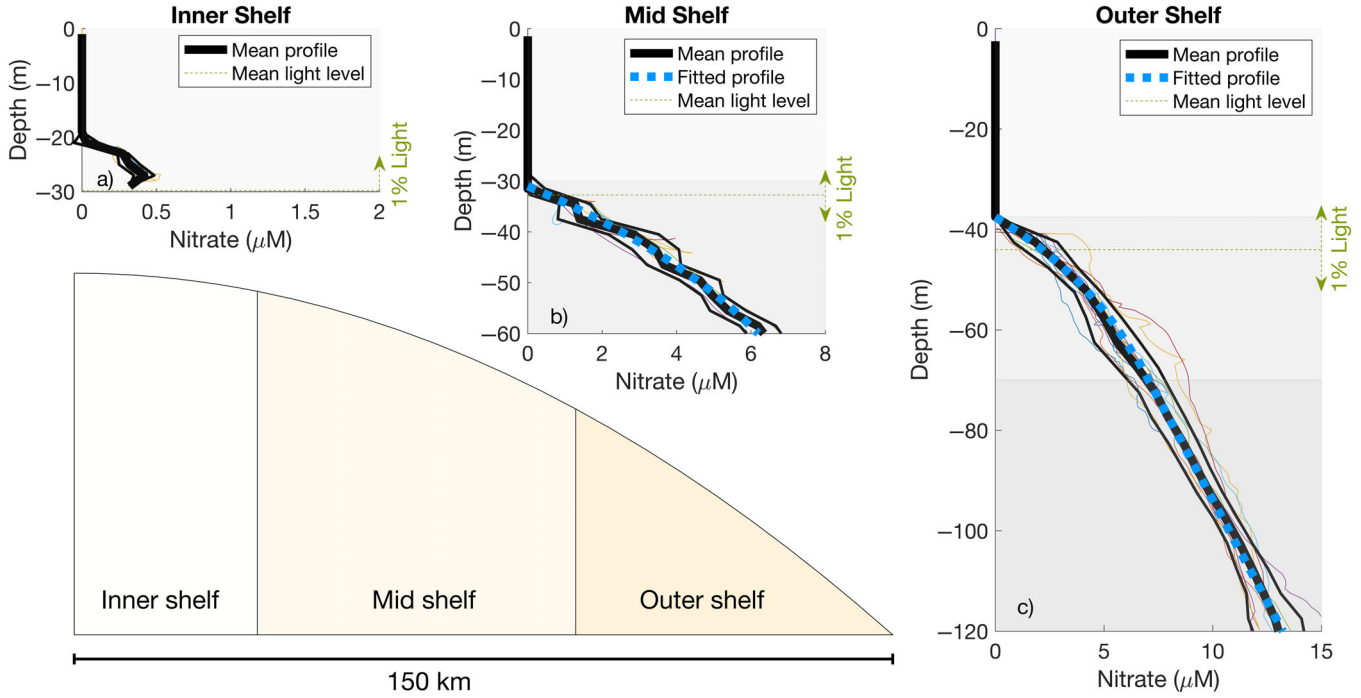

Fig. 5. Summertime section-mean nitrate profiles for the (**a**) inner shelf; (**b**) mid-shelf; and (**c**) outer shelf. Note that the ranges of the axes are different in each panel. The thick black lines are the section-mean nitrate profile, with the error range (defined by one standard deviation) indicated by the thin black lines. Fitted profiles are plotted in blue dashed lines. Colored spaghetti thin lines in the background show the individual station-mean nitrate profiles used in the averaging. Mean 1% light level depths are shown as horizontal green dashed lines, with arrows to the right of the panels annotating their variations in depth, which is mostly associated with variations among cross-shelf stations. The background gray shadings in (**a**–**c**) highlight different nitrate layers. The schematic on the lower left denotes the continental shelf with the background orange shadings (the same in Fig. 8c) representing the three cross-shelf sections.

In the summer, the nitracline depth, where nitrate concentration exhibits the largest vertical gradient, normally coincides with the vertical location where nitrate concentration transitions from being undetectable to detectable (Omand and Mahadevan 2015; Gong et al. 2017). All four summer cruises analyzed here show a consistent pattern of nitrate-density relationship: near-zero nitrate concentration at density < 24.5 kg m^{-3}, increasing nitrate concentration with density in the density range of ~ 24.5 to ~ 27 kg m^{-3}, and decreasing nitrate concentration with increasing density at density > 27 kg m^{-3} (Fig. 6a–d). Meanwhile, the density at which nitrate concentration starts to increase varies among the stations, and it generally occurs at lower densities at the inner shelf stations (red dots in Fig. 6a–d) than at the outer-shelf stations (blue dots in Fig. 6a–d). To illustrate this latitudinal dependency, we plot the density value at the nitracline against latitude (Fig. 6e). This relationship exhibits a linear trend consistent among the cruises, and a linear fit gives $\rho_{ni} = -0.85\text{Lat} + 59.88$, where ρ_{ni} is the density at the nitracline in kg m^{-3} and Lat is the latitude in degrees.

The mean vertical diffusivity profile estimated from the MacKinnon–Gregg method shows a general shape of decreasing values with increasing depth, characterized by $O(10^{-4})$ m^{-2} s^{-1} near the surface and $O(10^{-5})$ m^{-2} s^{-1} at depth (Fig. 7). The estimated mean diffusivities at the outer shelf are about two times higher than those at the mid-shelf. This is consistent with stronger internal wave activities at the shelf edge induced by strong interactions of tides and internal tides with the steep topography (e.g., Kelly and Nash 2010; Zhang et al. 2013). The general shape of the estimated diffusivity profiles is also consistent with results of observational studies (MacKinnon and Gregg 2005) and modeling work in the region (Zhang et al. 2013).

Since the vertical nitrate gradient is small due to the uniform distribution of nitrate at the inner shelf (Fig. 5a), inner shelf F_n is not calculated for further analysis. At the mid-shelf, the base of the euphotic zone is at 35 m (Fig. 5b), and F_n at that depth is $8.2 \pm 5.3 \times 10^{-6}$ mmol N m^{-2} s^{-1}. At the outer shelf, F_n at the base of the euphotic zone, 45 m deep (Fig. 5c), is $12.6 \pm 8.6 \times 10^{-6}$ mmol N m^{-2} s^{-1}. With the Redfield ratio of C : N = 106 : 16 (Redfield 1934), these upward fluxes of nitrate can be converted into upward carbon fluxes of 56 ± 36 mg C m^{-2} d^{-1} at the mid-shelf and 87 ± 58 mg C m^{-2} d^{-1} at the outer shelf.

Oxygen-based GPP and NCP estimates provide direct quantification of the overall biological productivity (weighted average of the past 3–5 d) in the near-surface euphotic zone of the NES. The multi-year summertime measurements exhibit a general trend of decreasing GPP toward offshore, with a mean

19395590, 2025, 2, Downloaded from https://aslopubs.onlinelibrary.wiley.com/doi/10.1002/lno.12765 by Mbl Whoi Library, Wiley Online Library on [21/05/2025]. See the Terms and Conditions (https://onlinelibrary.wiley.com/terms-and-conditions) on Wiley Online Library for rules of use; OA articles are governed by the applicable Creative Commons License

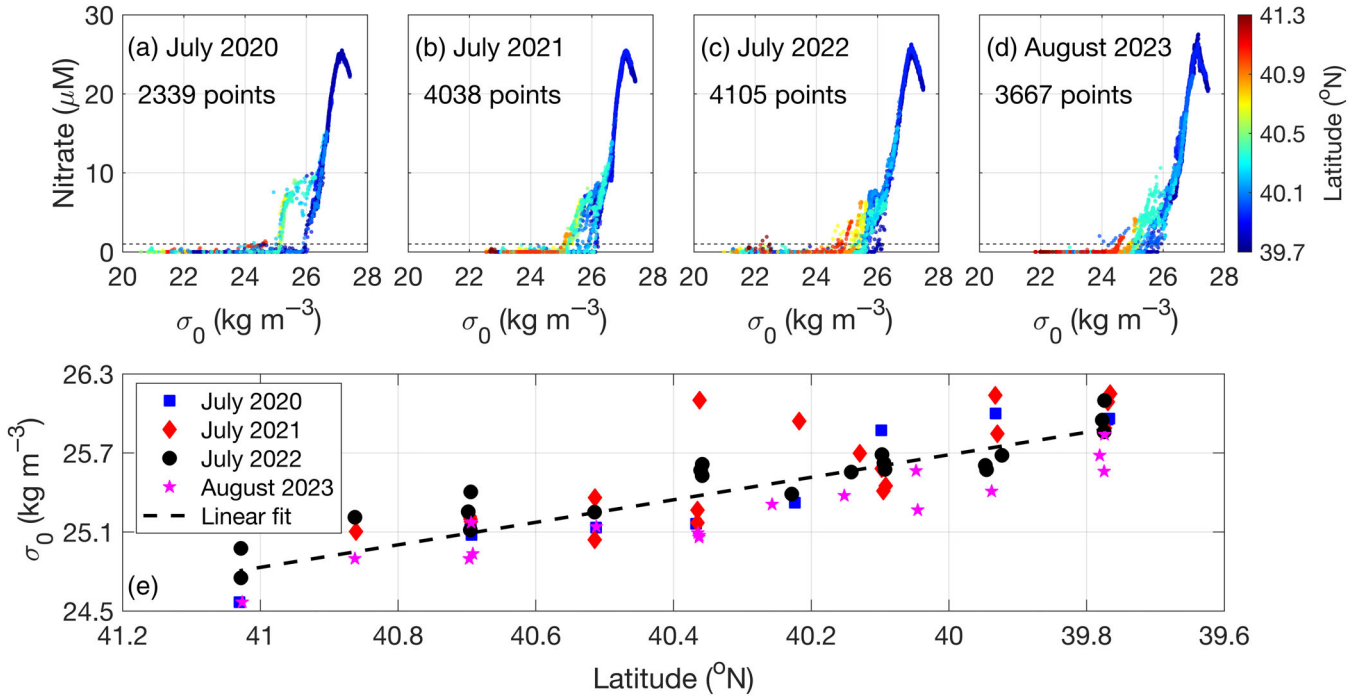

Fig. 6. (**a–d**) Nitrate-density relationships color-coded by latitude for four summer cruises with the horizontal dashed lines denoting the nitracline position; and (**e**) the density of the nitracline as a function of latitude.

value of 604 ± 139 mg C m^{-2} d^{-1} for the mid-shelf and 530 ± 101 mg C m^{-2} d^{-1} for the outer shelf (Fig. 8a). On the other hand, NCP does not show cross-shelf variation, with a mean value of 54 ± 15 mg C m^{-2} d^{-1} for the mid-shelf and 54 ± 14 mg C m^{-2} d^{-1} for the outer shelf (Fig. 8b). The NCP/GPP ratios are 0.09 ± 0.03 and 0.1 ± 0.03 for the mid- and outer shelf, respectively (Fig. 8c). *See* Supporting Information for the calculation of the error bar.

We now estimate the ratio of new production to total primary production in the euphotic zone by dividing the estimated vertical diffusive nitrate flux (F_n) at the base of the euphotic zone by the measured GPP in the euphotic zone. The ratios are 0.09 ± 0.06 and 0.14 ± 0.11 for the mid- and outer shelf, respectively (Fig. 8c). Here one major assumption is that the upward diffusive nitrate flux across the base of the euphotic zone is the dominant source of new nitrogen in

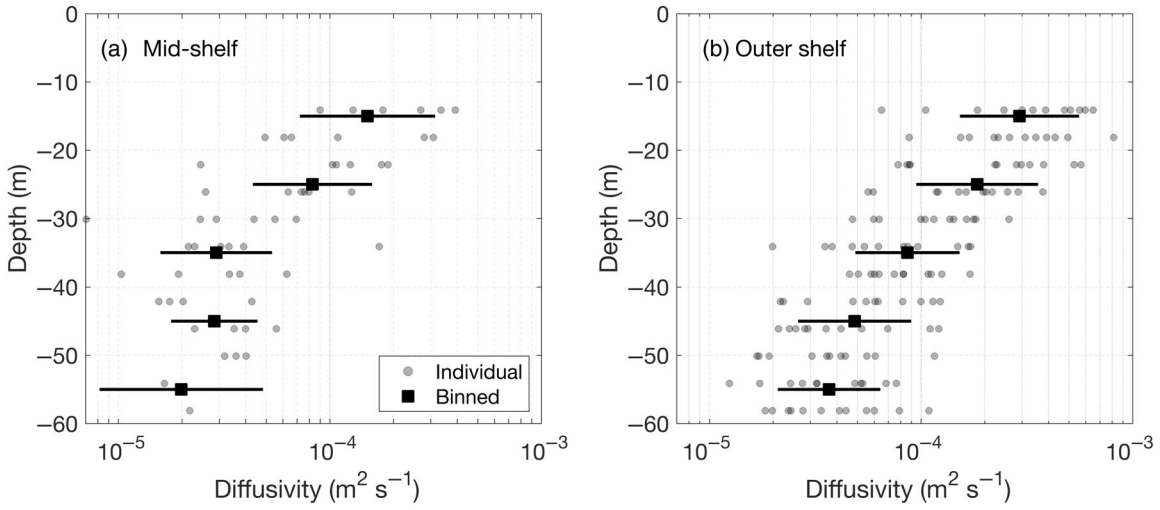

Fig. 7. Estimated vertical diffusivity at the (**a**) mid-shelf and (**b**) outer shelf. Dots are individual estimates for each depth at each station and black squares are the median diffusivity value within each 10-m vertical bin, with error bars (1 standard deviation of the log-transformed values) denoted by the black lines.

19395590, 2025, 2, Downloaded from https://aslopubs.onlinelibrary.wiley.com/doi/10.1002/lno.12765 by Mbl Whoi Library, Wiley Online Library on [21/05/2025]. See the Terms and Conditions (https://onlinelibrary.wiley.com/terms-and-conditions) on Wiley Online Library for rules of use; OA articles are governed by the applicable Creative Commons License

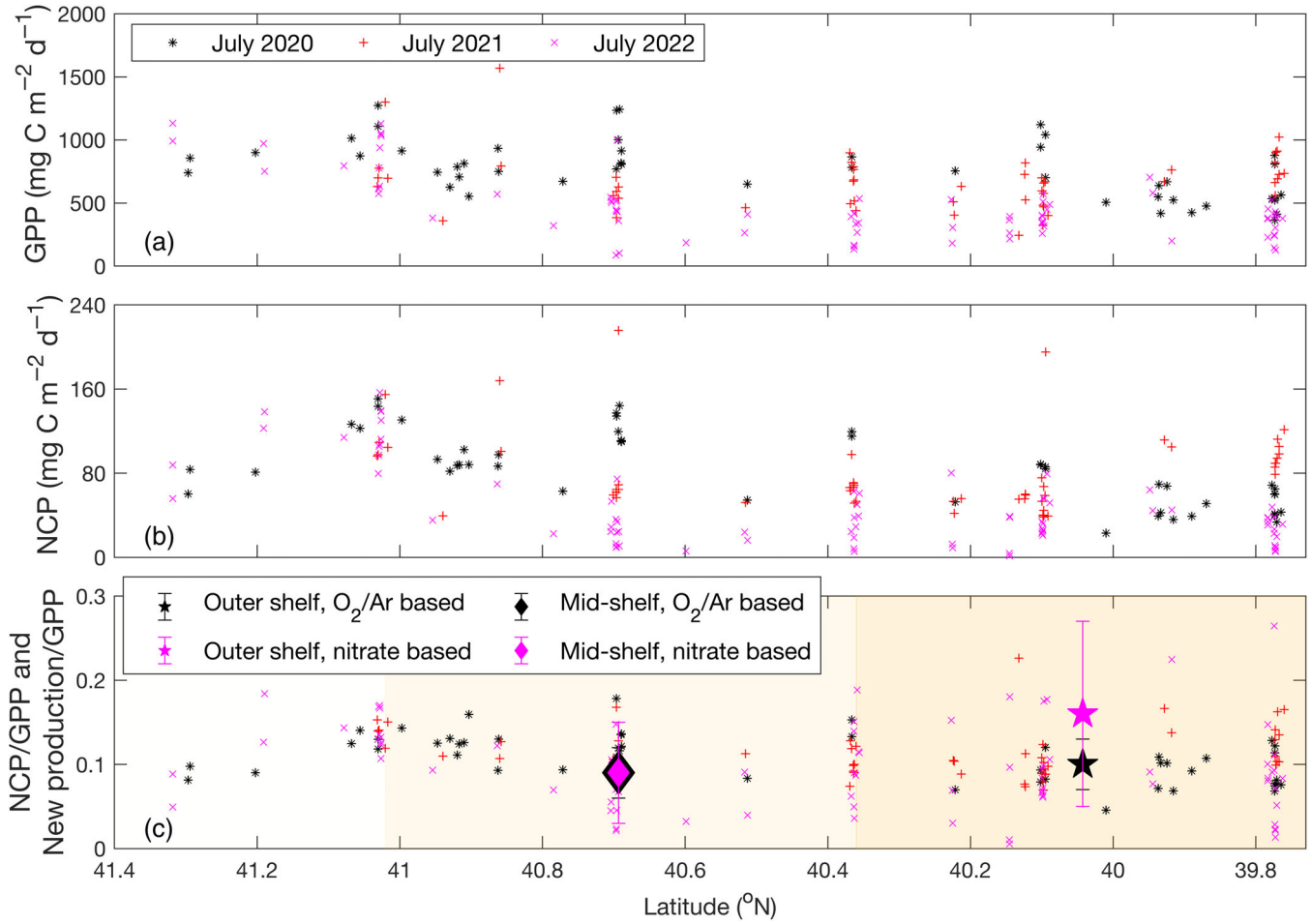

Fig. 8. Cross-shelf measurements of (**a**) gross primary production (GPP); (**b**) net community production (NCP); and (**c**) NCP/GPP and New production/GPP (f-ratio). Note that the mid- and outer-shelf regions are denoted by the different background orange colors in (**c**).

the nutrient-depleted euphotic zone to sustain new production. The validity of this assumption will be discussed in the next section. Overall, the measured summer mean NCP/GPP ratio and the estimated summer mean new production/GPP ratio (or in other words, NCP and new production) present a consistent pattern across a wide shelf area (Fig. 8c). Importantly, this consistent pattern is revealed by observational data from two independent approaches—one is based on the high-resolution SUNA-measured nitrate data, and the other is based on measurements of oxygen isotopes and oxygen/Ar ratios.

Discussion

The 4-yr high-resolution in situ measurements of physical and biogeochemical variables across the entire shelf allow us to (1) characterize the mean nitrate distribution in different cross-shelf sections of the NES during the summer time; (2) directly quantify rates of upward nutrient flux into the euphotic zone; and (3) establish a baseline to facilitate the detection of disturbance to the local biogeochemical fields. In the following section, we suggest constraining mechanisms to the nitrate profile, interpret the contribution of upward nitrate flux in sustaining primary production, and discuss the deviation of nitrate distribution during episodic disturbance events as compared to its more typical state.

Nitrate profile modulation processes

We now seek to demonstrate that nitrate profiles on the NES are modulated by both physical and biochemical processes, with relative contributions varying between distinct vertical layers of the profiles. The steady-state cross-shelf advection–diffusion equation for nitrate is:

$$w\frac{\partial n}{\partial z}+v\frac{\partial n}{\partial y}=\frac{\partial}{\partial z}\left(k_v\frac{\partial n}{\partial z}\right)-\text{Bio} \tag{9}$$

where, w and v are vertical and cross-shelf velocity, respectively, and Bio is the biological uptake rate of nitrate. Here, we assume the along-shelf gradient of properties is small (e.g., Zhang et al. 2013), and thus neglected in Eq. 9. Note

19395590, 2025, 2, Downloaded from https://aslopubs.onlinelibrary.wiley.com/doi/10.1002/lno.12765 by Mbl Whoi Library, Wiley Online Library on [21/05/2025]. See the Terms and Conditions (https://onlinelibrary.wiley.com/terms-and-conditions) on Wiley Online Library for rules of use; OA articles are governed by the applicable Creative Commons License

that the vertical mixing term, $\frac{\partial}{\partial z}(k_v\frac{\partial n}{\partial z})$, can be separated into two parts: vertical change of the nitrate concentration gradient, $k_v\frac{\partial^2 n}{\partial z^2}$, and vertical change of the vertical diffusivity, $\frac{\partial k_v}{\partial z}\frac{\partial n}{\partial z}$.

Within the surface euphotic zone, nitrate is near zero consistently across the continental shelf (Fig. 5). The sustained sharp nitracline suggests that the biological uptake rate of nitrate exceeds the vertical supply rate of nitrate in the euphotic zone (more evidence in the following section) and thus maintains the near-zero nitrate concentration in the surface layer.

The layer immediately below the surface layer in the mid- and outer shelf is characterized by an exponential increase of nitrate concentration with depth (Fig. 5b,c). The dominant balance that shapes this nitrate layer can be investigated by scaling the terms in Eq. 9. Taking representative values of w of $3\times10^{-6}\,\mathrm{m\,s^{-1}}$ (Zhang et al. 2011), v of $5\times10^{-3}\,\mathrm{m\,s^{-1}}$ (Zhang et al. 2011), $\frac{\partial n}{\partial y}$ of $3\times10^{-6}\,\mathrm{mmol\,N\,m^{-4}}$ (Fig. 5), $\frac{\partial n}{\partial z}$ of $0.2\,\mathrm{mmol\,N\,m^{-4}}$ (Fig. 5), $\frac{\partial^2 n}{\partial z^2}$ of $8\times10^{-3}\,\mathrm{mmol\,N\,m^{-5}}$ (Fig. 5), k_v of $4\times10^{-5}\,\mathrm{m^2\,s^{-1}}$ (Fig. 7), and Bio of $6.8\times10^{-8}\,\mathrm{mmol\,N\,m^{-3}\,s^{-1}}$ (approximated by and converted from the averaged NPP value between 0.1% and 1% light level depths, and C : N = 106 : 16), the vertical advection term ($w\frac{\partial n}{\partial z}$) and vertical diffusion term ($k_v\frac{\partial^2 n}{\partial z^2}$) are on the order of $10^{-7}\,\mathrm{mmol\,N\,m^{-3}\,s^{-1}}$. They are about one order of magnitude larger than both the cross-shore advection term ($v\frac{\partial n}{\partial y}$) and the biological uptake term (Bio). Note that contribution of the vertical variation of the diffusivity, $\frac{\partial k_v}{\partial z}\frac{\partial n}{\partial z}$, to the vertical diffusion term is several orders of magnitude smaller than $k_v\frac{\partial^2 n}{\partial z^2}$, because the vertical gradient of diffusivity $\frac{\partial k_v}{\partial z}\sim5\times10^{-7}\,\mathrm{m\,s^{-1}}$ is small in the exponential section of the nitrate profile (Fig. 7). Thus, we conclude that vertical advection and vertical diffusion are the two leading-order processes shaping the exponential profiles of nitrate concentration. That is,

$$w\frac{\partial n}{\partial z}\approx k_v\frac{\partial^2 n}{\partial z^2} \tag{10}$$

The analytical solution to Eq. 10 is $n=\alpha+\beta e^{\gamma z}$, where α, β, and γ are constants. Least-squares fits to the measured exponential profiles in the vertical sections give values of $\alpha=10.7$ and $9.9\,\mu\mathrm{M}$, $\beta=-27$ and $-36.2\,\mu\mathrm{M}$, $\gamma=0.03$ and $0.035\,\mathrm{m^{-1}}$ for the mid- and outer shelf, respectively. Because γ represents the ratio of w over k_v, its value can be combined with the value of k_v to provide an estimate of the mean vertical velocity, w. Following this idea, with $k_v=3\times10^{-5}$ and $5\times10^{-5}\,\mathrm{m^2\,s^{-1}}$, we obtain $w=0.08$ and $0.15\,\mathrm{m\,d^{-1}}$ for the mid- and outer shelf, respectively. These values are consistent with previous estimates of the mean upwelling velocity in the region (e.g., Zhang et al. 2011), providing a corroboration of our analysis.

NPP estimates support our conclusion that the biological uptake term (Bio) can be neglected in determining the leading-order steady state cross-shelf nitrate balance for the layer immediately below the euphotic zone. To demonstrate this, we quantify the fraction of the overall water column NPP occurring below the euphotic zone during 2020–2022, which can be expressed as:

$$\lambda=\frac{\Sigma_{i=1}^{q}\mathrm{NPP}(i)\times\delta z(i)}{\Sigma_{j=1}^{p}\mathrm{NPP}(j)\times\delta z(j)} \tag{11}$$

where q is the number of NPP measurements below the 1% light level, p is the number of NPP measurements over the entire water column, and δz is the vertical distance between two neighboring NPP measurements. We find that NPP below the euphotic zone consistently accounts for less than 2% of the overall NPP in the water column, suggesting that biological production and nutrient uptake are negligible below the euphotic zone.

In the lowest layer, which has a linear nitrate profile at the outer-shelf section, the nitrate balance is primarily modulated by cross-shore advection and vertical advection:

$$w\frac{\partial n}{\partial z}+v\frac{\partial n}{\partial y}\approx0 \tag{12}$$

Specifically, the mean onshore-directed cross-shore current, v, acts upon the cross-shore nitrate gradient, $\frac{\partial n}{\partial y}$, with higher nitrate onshore, and consequently reduces nitrate concentration in that layer. Analysis of the Ocean Observatories Initiative Pioneer Array acoustic Doppler current profiler data gives a mean onshore velocity at the depth range of 0.002–$0.009\,\mathrm{m\,s^{-1}}$, similar to the range of 0.005–$0.01\,\mathrm{m\,s^{-1}}$ reported in previous studies (e.g., Lentz 2008; Zhang et al. 2011); With the estimated $\frac{\partial n}{\partial y}$ of $\sim3.8\times10^{-5}\,\mathrm{mmol\,N\,m^{-4}}$, $\frac{\partial n}{\partial z}$ of $\sim0.13\,\mathrm{mmol\,N\,m^{-4}}$ (Fig. 5c), and w of $\sim1.7\times10^{-6}\,\mathrm{m\,s^{-1}}$ ($0.15\,\mathrm{m\,d^{-1}}$), we achieve a quantitative balance between the nitrate reduction due to onshore advection and the upward advection of nitrate, consistent with Eq. 12.

The summertime nitrate field exhibits a robust relationship with density during the summers sampled (Fig. 6a–d); moreover, density at the nitracline displays cross-shelf variations (Fig. 6a–d). Studies of mesoscale processes have demonstrated that nitrate surfaces generally align with density surfaces (e.g., Omand and Mahadevan 2013), and the nitrate-density (or nitrate-temperature) relationship has been used to infer nitrate from hydrographic measurements when in situ nitrate data are not available (e.g., McGillicuddy and Robinson 1997). Here, our analysis not only provides a quantitative summertime nitrate-density relationship for the NES, but also reveals the spatial variation of this relationship in this frontal zone. In particular, the cross-shelf variation of density at the nitracline is caused by the misalignment of the cross-shelf slope of the density surfaces and the isolume surfaces (e.g., Fig. 9c). Specifically, isopycnals are normally upward tilted with a cross-shore isobaric gradient of increasing values offshore (Fig. 9c). On the other hand, isolumes, for example, the 1% light level, tilt downward toward offshore (Figs. 5, 9c) due to the gradual reduction of the concentrations of organic

19395590, 2025, 2, Downloaded from https://aslopubs.onlinelibrary.wiley.com/doi/10.1002/lno.12765 by Mbl Whoi Library, Wiley Online Library on [21/05/2025]. See the Terms and Conditions (https://onlinelibrary.wiley.com/terms-and-conditions) on Wiley Online Library for rules of use; OA articles are governed by the applicable Creative Commons License

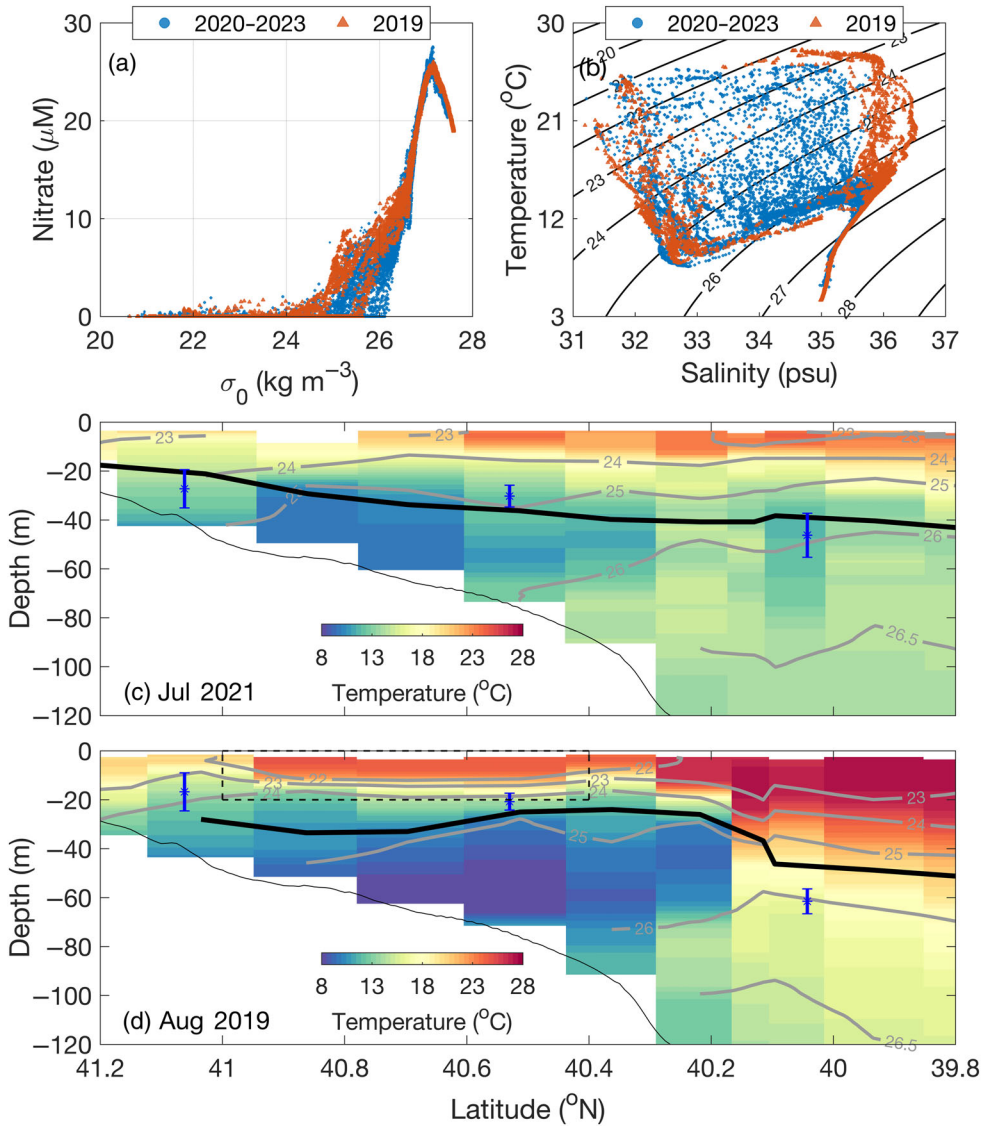

Fig. 9. Comparison of (**a**) nitrate-density relationships, (**b**) temperature-salinity relationships, and (**c** and **d**) cross-shelf temperature field in summer 2019 and the summers of 2020–2023. The black lines are density contours in b; In (**c** and **d**), the gray lines are isopycnals, the black lines denote the nitracline depth, the blue stars and the blue vertical bars represent the mean euphotic depths and the standard deviations at the inner, mid-, and outer shelf, respectively. The dashed box in d outlines the location of the diatom-diazotroph bloom. The fields shown in c represent mean conditions in summers of 2020–2023.

materials (Zhang et al. 2023). Consequently, the 1% isolume intercepts different isopycnals at different cross-shelf locations, which causes the gradual increase of the density at the base of the euphotic zone toward offshore (Fig. 9c). This increase in density of the 1% light level thus results in a latitudinal relationship between density and nitracline depth, reflecting the large-scale alignment between the euphotic zone depth and nitracline (e.g., black line and blue stars in Fig. 9c).

Nitrate budget and ecological implications

Detailed quantification of nitrate flux from different pathways into the euphotic zone allows a better understanding of the nitrogen cycle as well as the ecological function of nitrate in sustaining biological production. Thus, we aim to quantify the summertime nitrate budget of the euphotic zone over the NES. Nitrate input from the atmosphere into the ocean is presumably negligible (Nixon et al. 1996; Zhang et al. 2019). Thus, allochthonous nitrate input to the euphotic zone is dominated by lateral transport (i.e., cross-shore and alongshore nitrate flux) and vertical transport (i.e., vertical nitrate flux). Due to the fact that nitrate concentration is nearly zero in the euphotic zone over a broad NES area in summer (Fig. 5; Oliver et al. 2022), lateral transport in the euphotic zone can be neglected. Thus, nitrate input into the euphotic zone is dominated by the vertical nitrate flux, which includes two components—the vertical diffusive flux ($k_v \frac{\partial n}{\partial z}$) and vertical

19395590, 2025, 2, Downloaded from https://aslopubs.onlinelibrary.wiley.com/doi/10.1002/lno.12765 by Mbl Whoi Library, Wiley Online Library on [21/05/2025]. See the Terms and Conditions (https://onlinelibrary.wiley.com/terms-and-conditions) on Wiley Online Library for rules of use; OA articles are governed by the applicable Creative Commons License

advective flux (*wn*). At the base of the euphotic zone, w is $\sim 9.3 \times 10^{-7}\,\mathrm{m\,s^{-1}}$ for the mid-shelf and $\sim 1.7 \times 10^{-6}\,\mathrm{m\,s^{-1}}$ for the outer shelf (estimated above), and n is $\sim 1\,\mu\mathrm{M}$. This w and n give a vertical advective flux several times smaller than the vertical diffusive flux estimated above. Therefore, our analysis shows that the first-order contribution to the summertime new production in the euphotic zone comes from the vertical diffusive nitrate flux, which is about $56\,\mathrm{mg\ C\,m^{-2}\,d^{-1}}$ at the mid-shelf and $87\,\mathrm{mg\ C\,m^{-2}\,d^{-1}}$ at the outer shelf. These values are consistent with previous estimates in the NES waters (e.g., 4–67 $\mathrm{mg\ C\,m^{-2}\,d^{-1}}$; Harrison et al. 1983) and similar to the estimates in other shelf environments (e.g., 13–1372 $\mathrm{mg\ C\,m^{-2}\,d^{-1}}$; Chen 2003).

The ratio between new production and GPP quantifies the portion of total primary production that is fueled by "new" nitrogen vs. "regenerated" nitrogen. This ratio, the f-ratio, is a critical characterization of nitrogen budget in marine ecosystems (Eppley and Peterson 1979; Falkowski et al. 2003). Our results suggest that less than 15% of the summertime GPP is fueled by new nitrogen from below the euphotic zone over the mid- and outer shelf of the NES. This implies that the photoautotrophic community is sustained largely by regenerated nitrogen. Our result is consistent with the consensus in the literature that the "regenerated" production contributes more in sustaining the summertime total primary production over NES, as indicated by indirectly quantified ratios of new to total production of 0.1–0.5 (Harrison et al. 1983; Franks and Chen 2001). These indirect quantifications of the f-ratio use the total nitrogen uptake rate ($NO_3 + NH_4$) as an approximation of the total primary production, as originally suggested by Dugdale and Goering (1967) and followed in other recent studies (e.g., Fouilland et al. 2007; Flynn et al. 2023). Importantly, our work offers a direct and robust quantification of the f-ratio using long-term high-resolution nitrate and productivity data, with an uncertainty range narrower than that from previous work.

The other approach to quantify the new production vs. GPP is to compare NCP to GPP. One underlying assumption for this approach is that the targeted ecosystem is in steady state, where the new production is equivalent to NCP (*see* Falkowski et al. 2003 for more discussions). Our findings support this equivalency since nitrate-based new production and oxygen-based NCP are consistent with each other (Fig. 8). This consistency also serves as a validation of the results from two independent methods.

Following the idea that the NES over our target time and region is in steady state, the new production (or NCP) is also equivalent to the export production, which quantifies the amount of organic material being exported from the euphotic layer to deeper waters or the benthos (Sigman and Hain 2012). Therefore, the export ratio, that is, the ratio of export production to total primary production, the e-ratio (Murray et al. 1989), in the summertime NES is about 10–15% at the euphotic depth, meaning that a small portion of the organic material leaves the euphotic zone. As organic matter export is a type of carbon sink of the surface ocean, which has to be resupplied by carbon drawdown from the atmosphere, the estimated export ratio helps constrain the air-sea carbon fluxes in the summertime NES. These better-constrained air–sea carbon fluxes would help improve our understanding of the ocean's potential to take up atmospheric CO_2 and modulate the changing climate. Furthermore, it is the new supply of nitrogen that allows production to be available for transfer to higher trophic levels or be exported to the deep ocean or benthos (Dugdale and Goering 1967), and thus crucial for providing energy to those components of the ecosystem.

The export ratio estimated from our observations on the NES is notably lower than that from the empirical relationship in the classic work of Eppley and Peterson (1979) (0.26). Our analysis of the NES data serves as a good example to demonstrate that using empirical relationships to estimate the export ratio on the global scale is not appropriate considering the regional and seasonal heterogeneity of this property (as also illustrated in Buesseler et al. 2020 and references within). Therefore, we advocate more systematical quantification of the f-ratio (and export ratio) at a spatial and temporal resolution that are comparable to the scale of the leading order variance of the ocean state. The feasibility of using ship-board high-resolution in situ nitrate measurements to quantify these ratios on the continental shelf scale within a specific season, as demonstrated by our work, opens up opportunities for similar analysis with other observation datasets. These observational data can be collected from, for example, routine survey cruises (e.g., marine-based LTER sites, and GO-SHIP cruises), biogeochemical floats (e.g., Biogeochemical Argo), moorings, and gliders. Multi-platform high-resolution nitrate observations would provide unprecedented opportunities to study spatial distribution and temporal variations of the f-ratio (and export ratio), as well as support further improvements of the parameterizations of these two ratios in numerical models, which is crucial for climate predictions.

Disturbances

The NES is experiencing physical and ecological disturbances including frequent marine heat waves (e.g., Pershing et al. 2018), widespread intrusion of slope and Gulf Stream waters (e.g., Gawarkiewicz et al. 2022), and anomalous episodic blooms of phytoplankton (e.g., Smith et al. 2021; Castillo Cieza et al. 2024). These disturbances have the potential to alter the local ecosystem and biogeochemical functions.

Over the sampled summers of the NES-LTER, the summer of 2019 stands out as anomalous relative to other summers. As documented by Castillo Cieza et al. (2024), an unusual diatom-diazotroph bloom occupied the surface layer (top 20 m) of the mid-shelf waters in August 2019. They showed that there was a dramatic shift in the planktonic community composition (from the dominance of small $< 5\,\mu$m cells to large $> 20\,\mu$m cells of *Hemiaulus* bloom) and associated

19395590, 2025, 2, Downloaded from https://aslopubs.onlinelibrary.wiley.com/doi/10.1002/lno.12765 by Mbl Whoi Library, Wiley Online Library on [21/05/2025]. See the Terms and Conditions (https://onlinelibrary.wiley.com/terms-and-conditions) on Wiley Online Library for rules of use; OA articles are governed by the applicable Creative Commons License

changes in the oceanic productivity, compared to conditions in the same geographic area during summers in the adjacent years. Here we build upon the previous work and discuss how such a synoptic disturbance event, that is, anomalous bloom with N_2 fixing symbionts, co-occurs with significant deviations of the local physical and nitrate fields from their climatological means.

Nitrate distribution and water mass properties on the shelf were notably different during the summer of 2019 compared to other summers (2020–2023). The nitrate-density relationship (specifically for nitrate less than 12 μM) was shifted to a lower density range in the summer of 2019, and densities at the nitracline were lower by ~ 0.5 kg m^{-3} compared to other summers (Figs. 6a–d, 9a). We here propose a two-part explanation for this change in the nitrate-density relationship. First, for shelf regions with latitude greater than 40.2°N, the euphotic zone in 2019 was much shallower (by ~ 11 m at the inner shelf and ~ 10 m at the mid-shelf) than those during summers 2020–2023 (Fig. 9c,d). This shrinking of the euphotic zone was likely due to the elevated light attenuation by the near-surface bloom (Fig. 9d). Consequently, the shoaling euphotic zone led to the nitracline intercepting a shallower density layer than in other years. Meanwhile, the N_2-fixing symbionts observed during the bloom could also possibly result in elevated nitrate concentration in the near-surface mid-shelf water. Second, in summer 2019 an intrusion of the Gulf Stream water occurred on the outer shelf, with salinity of the intruding water higher than 36 psu, totally distinct from salinity of the outer-shelf water in other summers sampled (Fig. 9b). This intruding of Gulf Stream water occupied the upper ~ 40 m, and pushed isopycnals downward, leading to the nitracline intercepting a shallower isopycnal (Fig. 9d).

Together, these changes in the physical and biogeochemical patterns in summer 2019 indicate that synoptic disturbances to the NES can cause substantial deviations in nutrient distribution from the climatological mean. Alteration of the nutrient distribution could, in turn, affect ecosystem dynamics on temporal and spatial scales beyond those of the initial disturbance. The compilation of a suite of climatological metrics, such as the cross-shelf nitracline-latitude relationship (Fig. 6e), the nitrate-density relationship (Fig. 9a), and diffusivity profiles (Fig. 7), can facilitate the identification of disturbance events and help evaluate their ecological and biogeochemical impacts. This summer 2019 data serves as a case study highlighting the power of this type of analysis in future studies that are enabled by long-term high-resolution physical and biogeochemical measurements.

Conclusion

In summary, through analyzing repeatedly measured physical and biogeochemical properties of waters on the Northeast U.S. Shelf in 2019–2023, we are able to (1) characterize the average summertime nitrate distribution and examine its constraining processes; (2) directly quantify upward nitrate flux into the euphotic zone; (3) estimate the contribution of new production (via vertical diffusive nitrate flux) to total primary production in the euphotic zone, that is, the f-ratio; and (4) capture the nitrate distribution anomaly during a synoptic disturbance event. This work is largely facilitated by the SUNA-measured in situ high-resolution vertical nitrate profiles along a specific NES transect with adequate cross- and along-shelf spatial coverages as well as multi-year temporal coverage.

We show that the nitrate concentration in the euphotic zone on the NES during summer is primarily controlled by biological processes, while physical processes, namely vertical advection, vertical diffusion, and cross-shelf advection modulate the nitrate profile below the euphotic zone. Our results suggest that the supply of new nitrogen to the euphotic zone over the NES in summer is dominated by vertical diffusive nitrate flux, which fuels 10–15% of the total production of the shelf ecosystem. Notably, this nitrate-based new production estimate is consistent with concurrent but independent gas-tracer-based estimates of NCP. This consistency supports the assumption that the NES over the summers in 2020–2023 is approximately in a steady state regarding the balance of allochthonous nutrient inputs to the euphotic zone and the organic matter being produced there. This consistency further implies that the export efficiency of the NES in summer is fairly low. Only 10–15% of the organic matter produced in summer is exported out of the euphotic zone. We would like to emphasize that our analysis is applicable to other dataset with similar observations taken from other sea-going opportunities and platforms, such as routine survey cruises, biogeochemical floats, and gliders. These nitrate measurements, characterized as high vertical resolution, and more spatial and temporal coverages, would ultimately improve our understanding of the nutrient cycling and ecosystem dynamics over a scale that is impossible before.

The summertime mean nitrate distribution presented here, including the nitrate-density relationship and nitracline depth, provides an important baseline for the identification of not only episodic disturbances (e.g., the 2019 *Hemiaulus* bloom; Castillo Cieza et al. 2024) but also long-term change in the shelf ecosystem. This is crucial because the NES is undergoing dramatic changes, including warming sea surface temperature and increasing stratification (e.g., Saba et al. 2016), and shifts of the biological community (e.g., Kleisner et al. 2017), at a rate faster than most other ocean regions (Pershing et al. 2015). Studies have shown that changes in the hydrographic condition can lead to changes in the nutrient field, which then alters the community composition of higher trophic levels (Mountain and Kane 2010; Zang et al. 2021). Without enough observations simultaneously spanning hydrography, biogeochemistry, and food web compositions, it remains difficult to accurately quantify the linkage among them, which in turn hinders accurate representation of the hydrographic influence and community response in ecological

19395590, 2025, 2, Downloaded from https://aslopubs.onlinelibrary.wiley.com/doi/10.1002/lno.12765 by Mbl Whoi Library, Wiley Online Library on [21/05/2025]. See the Terms and Conditions (https://onlinelibrary.wiley.com/terms-and-conditions) on Wiley Online Library for rules of use; OA articles are governed by the applicable Creative Commons License

models. Sustained monitoring of the NES is thus an indispensable approach to collecting information to characterize the changes as well as understand drivers of the local ecosystem dynamics, such as nutrient transport pathways. This information will support further improvement of the predictions of the marine ecosystem under the future climate.

Data availability statement

All in situ data are available via the EDI data repository at https://portal.edirepository.org/nis/browseServlet?searchValue=NES, last accessed: June 4, 2024. Raw gas tracer data used for calculating NCP and gross oxygen production are available at https://portal.edirepository.org/nis/mapbrowse?packageid=knb-lter-nes.6.3, last accessed: June 4, 2024. NPP data are available at https://portal.edirepository.org/nis/metadataviewer?packageid=knb-lter-nes.16.4, last accessed: June 4, 2024. Quality-controlled SUNA nitrate data are available at https://doi.org/10.25921/8pea-z372.

References

Bisagni, J. J. 2003. Seasonal variability of nitrate supply and potential new production in the Gulf of Maine and Georges Bank regions. J. Geophys. Res. Oceans **108**: 8015. doi:10.1029/2001JC001136

Buesseler, K. O., P. W. Boyd, E. E. Black, and D. A. Siegel. 2020. Metrics that matter for assessing the ocean biological carbon pump. Proc. Natl. Acad. Sci. **117**: 9679–9687. doi:10.1073/pnas.1918114117

Caldwell, D. R., and J. N. Mourn. 1995. Turbulence and mixing in the ocean. Rev. Geophys. **33**: 1385–1394. doi:10.1029/95RG00123

Cassar, N., B. A. Barnett, M. L. Bender, J. Kaiser, R. C. Hamme, and B. Tilbrook. 2009. Continuous high-frequency dissolved O_2/Ar measurements by equilibrator inlet mass spectrometry. Anal. Chem. **81**: 1855–1864. doi:10.1021/ac802300u

Castillo Cieza, S. A., and others. 2024. Unusual *Hemiaulus* bloom influences ocean productivity in Northeast U.S. Shelf Waters. Biogeosciences **21**: 1235–1257. doi:10.5194/bg-21-1235-2024

Chen, C.-T. A. 2003. New vs. export production on the continental shelf. Deep-Sea Res. II Top. Stud. Oceanogr. **50**: 1327–1333. doi:10.1016/S0967-0645(03)00026-2

Colosi, J. A., R. C. Beardsley, J. F. Lynch, G. Gawarkiewicz, C.-S. Chiu, and A. Scotti. 2001. Observations of nonlinear internal waves on the outer New England continental shelf during the summer Shelfbreak Primer study. J. Geophys. Res. Oceans **106**: 9587–9601. doi:10.1029/2000JC900124

Dugdale, R. C., and J. J. Goering. 1967. Uptake of new and regenerated forms of nitrogen in primary productivity. Limnol. Oceanogr. **12**: 196–206. doi:10.4319/lo.1967.12.2.0196

Eppley, R. W., and B. J. Peterson. 1979. Particulate organic matter flux and planktonic new production in the deep ocean. Nature **282**: 677–680. doi:10.1038/282677a0

Falkowski, P. G., E. A. Laws, R. T. Barber, and J. W. Murray. 2003. Phytoplankton and their role in primary, new, and export production, p. 99–121. *In* M. J. R. Fasham [ed.], Ocean biogeochemistry. Springer Berlin Heidelberg.

Fennel, K., J. Wilkin, J. Levin, J. Moisan, J. O'Reilly, and D. Haidvogel. 2006. Nitrogen cycling in the Middle Atlantic Bight: Results from a three-dimensional model and implications for the North Atlantic nitrogen budget. Global Biogeochem. Cycles **20**: 2005GB002456. doi:10.1029/2005GB002456

Flynn, R. F., and others. 2023. Nanoplankton: The dominant vector for carbon export across the Atlantic Southern Ocean in spring. Sci. Adv. **9**: eadi3059. doi:10.1126/sciadv.adi3059

Fontaine, D. N., P. Marrec, S. Menden-Deuer, H. M. Sosik, and T. A. Rynearson. 2025. Time series of phytoplankton net primary production reveals intense interannual variability and size-dependent chlorophyll-specific productivity on a continental shelf. Limnol. Oceanogr. **70**: 203–216. doi:10.1002/lno.12749

Fouilland, E., M. Gosselin, R. B. Rivkin, C. Vasseur, and B. Mostajir. 2007. Nitrogen uptake by heterotrophic bacteria and phytoplankton in Arctic surface waters. J. Plankton Res. **29**: 369–376. doi:10.1093/plankt/fbm022

Franks, P. J. S., and C. Chen. 2001. A 3-D prognostic numerical model study of the Georges Bank ecosystem. Part II: Biological-physical model. Deep-Sea Res. II Top. Stud. Oceanogr. **48**: 457–482.

Garcia, H. E., and L. I. Gordon. 1992. Oxygen solubility in seawater: Better fitting equations. Limnol. Oceanogr. **37**: 1307–1312. doi:10.4319/lo.1992.37.6.1307

Gawarkiewicz, G., and A. J. Plueddemann. 2020. Scientific rationale and conceptual design of a process-oriented shelfbreak observatory: The OOI Pioneer Array. J. Oper. Oceanogr. **13**: 19–36. doi:10.1080/1755876X.2019.1679609

Gawarkiewicz, G., P. Fratantoni, F. Bahr, and A. Ellertson. 2022. Increasing frequency of mid-depth salinity maximum intrusions in the Middle Atlantic Bight. J. Geophys. Res. Oceans **127**: e2021JC018233. doi:10.1029/2021JC018233

Gilbey, J., and others. 2021. The early marine distribution of Atlantic salmon in the north-east Atlantic: A genetically informed stock-specific synthesis. Fish Fish. **22**: 1274–1306. doi:10.1111/faf.12587

Gong, X., W. Jiang, L. Wang, H. Gao, E. Boss, X. Yao, S.-J. Kao, and J. Shi. 2017. Analytical solution of the nitracline with the evolution of subsurface chlorophyll maximum in stratified water columns. Biogeosciences **14**: 2371–2386. doi:10.5194/bg-14-2371-2017

Gregg, M. C., E. A. D'Asaro, J. J. Riley, and E. Kunze. 2018. Mixing efficiency in the ocean. Ann. Rev. Mar. Sci. **10**: 443–473. doi:10.1146/annurev-marine-121916-063643

19395590, 2025, 2, Downloaded from https://aslopubs.onlinelibrary.wiley.com/doi/10.1002/lno.12765 by Mbl Whoi Library, Wiley Online Library on [21/05/2025]. See the Terms and Conditions (https://onlinelibrary.wiley.com/terms-and-conditions) on Wiley Online Library for rules of use; OA articles are governed by the applicable Creative Commons License

Hales, B., D. Hebert, and J. Marra. 2009. Turbulent supply of nutrients to phytoplankton at the New England shelf break front. J. Geophys. Res. Oceans **114**: 2008JC005011. doi:10.1029/2008JC005011

Hama, T., T. Miyazaki, Y. Ogawa, T. Iwakuma, M. Takahashi, A. Otsuki, and S. Ichimura. 1983. Measurement of photosynthetic production of a marine phytoplankton population using a stable 13C isotope. Mar. Biol. **73**: 31–36. doi:10.1007/BF00396282

Hamme, R. C., and S. R. Emerson. 2004. The solubility of neon, nitrogen and argon in distilled water and seawater. Deep-Sea Res. I Oceanogr. Res. Pap. **51**: 1517–1528. doi:10.1016/j.dsr.2004.06.009

Harrison, W. G., D. Douglas, P. Falkowski, G. Rowe, and J. Vidal. 1983. Summer nutrient dynamics of the Middle Atlantic Bight: Nitrogen uptake and regeneration. J. Plankton Res. **5**: 539–556. doi:10.1093/plankt/5.4.539

Henyey, F. S., J. Wright, and S. M. Flatté. 1986. Energy and action flow through the internal wave field: An eikonal approach. J. Geophys. Res. Oceans **91**: 8487–8495. doi:10.1029/JC091iC07p08487

Honda, I. A., R. Ji, and A. R. Solow. 2023. Spatially varying plankton synchrony patterns at seasonal and interannual scales in a well-connected shelf sea. Limnol. Oceanogr. Letters **8**: 906–915. doi:10.1002/lol2.10348

Jemison, L. A., G. W. Pendleton, K. K. Hastings, J. M. Maniscalco, and L. W. Fritz. 2018. Spatial distribution, movements, and geographic range of Steller sea lions (*Eumetopias jubatus*) in Alaska. PLoS One **13**: e0208093. doi:10.1371/journal.pone.0208093

Juranek, L. W., and P. D. Quay. 2013. Using triple isotopes of dissolved oxygen to evaluate global marine productivity. Ann. Rev. Mar. Sci. **5**: 503–524. doi:10.1146/annurev-marine-121211-172430

Kelly, S. M., and J. D. Nash. 2010. Internal-tide generation and destruction by shoaling internal tides. Geophys. Res. Lett. **37**: L23611. doi:10.1029/2010GL045598

Ketchum, B. H., R. F. Vaccaro, and N. Corwin. 1958. The annual cycle of phosphorus and nitrogen in New England coastal waters. J. Mar. Res. **17**: 282–301.

Kistler, R., and others. 2001. The NCEP–NCAR 50-year reanalysis: Monthly means CD-ROM and documentation. Bull. Am. Meteorol. Soc. **82**: 247–268. doi:10.1175/1520-0477(2001)082<0247:TNNYRM>2.3.CO;2

Kleisner, K. M., M. J. Fogarty, S. McGee, J. A. Hare, S. Moret, C. T. Perretti, and V. S. Saba. 2017. Marine species distribution shifts on the U.S. Northeast Continental Shelf under continued ocean warming. Prog. Oceanogr. **153**: 24–36. doi:10.1016/j.pocean.2017.04.001

Lentz, S. J. 2008. Observations and a model of the mean circulation over the Middle Atlantic Bight continental shelf. J. Phys. Oceanogr. **38**: 1203–1221. doi:10.1175/2007JPO3768.1

Longhurst, A., S. Sathyendranath, T. Platt, and C. Caverhill. 1995. An estimate of global primary production in the ocean from satellite radiometer data. J. Plankton Res. **17**: 1245–1271. doi:10.1093/plankt/17.6.1245

MacKinnon, J. A., and M. C. Gregg. 2005. Spring mixing: Turbulence and internal waves during restratification on the New England shelf. J. Phys. Oceanogr. **35**: 2425–2443. doi:10.1175/JPO2821.1

Marrec, P., H. McNair, G. Franzè, F. Morison, J. P. Strock, and S. Menden-Deuer. 2021. Seasonal variability in planktonic food web structure and function of the Northeast U.S. Shelf. Limnol. Oceanogr. **66**: 1440–1458. doi:10.1002/lno.11696

McGillicuddy, D. J., and A. R. Robinson. 1997. Eddy-induced nutrient supply and new production in the Sargasso Sea. Deep-Sea Res. I Oceanogr. Res. Pap. **44**: 1427–1450. doi:10.1016/S0967-0637(97)00024-1

Mountain, D. G. 2003. Variability in the properties of shelf water in the Middle Atlantic Bight, 1977–1999. J. Geophys. Res. Oceans **108**: 3014. doi:10.1029/2001JC001044

Mountain, D. G., and J. Kane. 2010. Major changes in the Georges Bank ecosystem, 1980s to the 1990s. Mar. Ecol. Prog. Ser. **398**: 81–91.

Murray, J. W., J. N. Downs, S. Strom, C.-L. Wei, and H. W. Jannasch. 1989. Nutrient assimilation, export production and 234Th scavenging in the eastern equatorial Pacific. Deep-Sea Res. I Oceanogr. Res. Pap. **36**: 1471–1489. doi:10.1016/0198-0149(89)90052-6

National Marine Fisheries Service. 2021. Fisheries economics of the United States, 2018. NOAA Tech. Memo. NMFS-F/SPO-225A. U.S. Department of Commerce.

Nixon, S. W., and others. 1996. The fate of nitrogen and phosphorus at the land-sea margin of the North Atlantic Ocean. Biogeochemistry **35**: 141–180. doi:10.1007/BF02179826

O'Reilly, J. E., and C. Zetlin. 1998. Season, horizontal, and vertical distribution of phytoplankton chlorophyll *a* in the northeast U.S. continental shelf ecosystem. U.S. Department of Commerce.

Oliver, H., W. G. Zhang, K. M. Archibald, A. J. Hirzel, W. O. Smith, H. M. Sosik, R. H. R. Stanley, and D. J. McGillicuddy. 2022. Ephemeral surface chlorophyll enhancement at the New England shelf break driven by Ekman restratification. J. Geophys. Res. Oceans **127**: e2021JC017715. doi:10.1029/2021JC017715

Omand, M. M., F. Feddersen, R. T. Guza, and P. J. S. Franks. 2012. Episodic vertical nutrient fluxes and nearshore phytoplankton blooms in Southern California. Limnol. Oceanogr. **57**: 1673–1688. doi:10.4319/lo.2012.57.6.1673

Omand, M. M., and A. Mahadevan. 2013. Large-scale alignment of oceanic nitrate and density: Nitrate-density alignment. J. Geophys. Res. Oceans **118**: 5322–5332. doi:10.1002/jgrc.20379

Omand, M. M., and A. Mahadevan. 2015. The shape of the oceanic nitracline. Biogeosciences **12**: 3273–3287. doi:10.5194/bg-12-3273-2015

19395590, 2025, 2, Downloaded from https://aslopubs.onlinelibrary.wiley.com/doi/10.1002/lno.12765 by Mbl Whoi Library, Wiley Online Library on [21/05/2025]. See the Terms and Conditions (https://onlinelibrary.wiley.com/terms-and-conditions) on Wiley Online Library for rules of use; OA articles are governed by the applicable Creative Commons License

Osborn, T. R. 1980. Estimates of the local rate of vertical diffusion from dissipation measurements. J. Phys. Oceanogr. **10**: 83–89. doi:10.1175/1520-0485(1980)010<0083:EOTLRO>2.0.CO;2

Pershing, A. J., and others. 2015. Slow adaptation in the face of rapid warming leads to collapse of the Gulf of Maine cod fishery. Science **350**: 809–812. doi:10.1126/science.aac9819

Pershing, A. J., K. E. Mills, A. M. Dayton, B. S. Franklin, and B. T. Kennedy. 2018. Evidence for adaptation from the 2016 marine heatwave in the Northwest Atlantic Ocean. Oceanography **31**: 152–161.

Plant, J. N., C. M. Sakamoto, K. S. Johnson, T. L. Maurer, and M. B. Bif. 2023. Updated temperature correction for computing seawater nitrate with in situ ultraviolet spectrophotometer and submersible ultraviolet nitrate analyzer nitrate sensors. Limnol. Oceanogr.: Methods **21**: 581–593. doi:10.1002/lom3.10566

Prokopenko, M. G., O. M. Pauluis, J. Granger, and L. Y. Yeung. 2011. Exact evaluation of gross photosynthetic production from the oxygen triple-isotope composition of O2: Implications for the net-to-gross primary production ratios. Geophys. Res. Lett. **38**. doi:10.1029/2011GL047652

Record, N. R., and others. 2019. Rapid climate-driven circulation changes threaten conservation of endangered North Atlantic right whales. Oceanography **32**: 162–169.

Redfield, A. C. 1934. On the proportions of organic derivatives in sea water and their relation to the composition of plankton, p. 176–192. *In* James Johnstone Memorial Volume. University Press of Liverpool.

Saba, V. S., and others. 2016. Enhanced warming of the Northwest Atlantic Ocean under climate change. J. Geophys. Res. Oceans **121**: 118–132. doi:10.1002/2015JC011346

Sakamoto, C. M., K. S. Johnson, and L. J. Coletti. 2009. Improved algorithm for the computation of nitrate concentrations in seawater using an in situ ultraviolet spectrophotometer. Limnol. Oceanogr.: Methods **7**: 132–143. doi:10.4319/lom.2009.7.132

Sakamoto, C. M., K. S. Johnson, L. J. Coletti, and H. W. Jannasch. 2017. Pressure correction for the computation of nitrate concentrations in seawater using an in situ ultraviolet spectrophotometer. Limnol. Oceanogr.: Methods **15**: 897–902. doi:10.1002/lom3.10209

Sedwick, P. N., P. W. Bernhardt, M. R. Mulholland, R. G. Najjar, L. M. Blumen, B. M. Sohst, C. Sookhdeo, and B. Widner. 2018. Assessing phytoplankton nutritional status and potential impact of wet deposition in seasonally oligotrophic waters of the Mid-Atlantic Bight. Geophys. Res. Lett. **45**: 3203–3211. doi:10.1002/2017GL075361

Sherman, K., J. Kane, S. Murawski, W. Overholtz, and A. Solow. 2002. The U.S. northeast shelf large marine ecosystem: Zooplankton trends in fish biomass recovery, p. 195–215. *In* K. Sherman and H. R. Skjoldal [eds.], Large marine ecosystems. Elsevier.

Sigman, D. M., and M. P. Hain. 2012. The biological productivity of the ocean. Nat. Educ. Knowl. **3**: 21.

Smith, W. O., Jr., and others. 2021. A regional, early spring bloom of *Phaeocystis pouchetii* on the New England continental shelf. J. Geophys. Res. Oceans **126**: e2020JC016856. doi:10.1029/2020JC016856

Stanley, R. H. R., W. J. Jenkins, D. E. Lott III, and S. C. Doney. 2009. Noble gas constraints on air-sea gas exchange and bubble fluxes. J. Geophys. Res. Oceans **114**: C11020. doi:10.1029/2009JC005396

Stevens, B. L. F., E. T. Crockford, E. E. Peacock, M. G. Neubert, and H. M. Sosik. 2023. Temperature regulates *Synechococcus* population dynamics seasonally and across the continental shelf. Limnol. Oceanogr. Letters **9**: 183–190. doi:10.1002/lol2.10331

Townsend, D. W. 1998. Sources and cycling of nitrogen in the Gulf of Maine. J. Mar. Syst. **16**: 283–295. doi:10.1016/S0924-7963(97)00024-9

Townsend, D. W., N. R. Pettigrew, M. A. Thomas, M. G. Neary, D. J. McGillicuddy, and J. O'Donnell. 2015. Water masses and nutrient sources to the Gulf of Maine. J. Mar. Res. **73**: 93–122. doi:10.1357/002224015815848811

van der Lee, E. M., and L. Umlauf. 2011. Internal wave mixing in the Baltic Sea: Near-inertial waves in the absence of tides. J. Geophys. Res. Oceans **116**: C10016. doi:10.1029/2011JC007072

Zang, Z., R. Ji, Z. Feng, C. Chen, S. Li, and C. S. Davis. 2021. Spatially varying phytoplankton seasonality on the Northwest Atlantic Shelf: A model-based assessment of patterns, drivers, and implications. ICES J. Mar. Sci. **78**: 1920–1934. doi:10.1093/icesjms/fsab102

Zang, Z., R. Ji, D. R. Hart, C. Chen, L. Zhao, and C. S. Davis. 2022. Modeling Atlantic sea scallop (*Placopecten magellanicus*) scope for growth on the Northeast U.S. Shelf. Fish. Oceanogr. **31**: 271–290. doi:10.1111/fog.12577

Zhang, W. G., G. G. Gawarkiewicz, D. J. McGillicuddy, and J. L. Wilkin. 2011. Climatological mean circulation at the New England shelf break. J. Phys. Oceanogr. **41**: 1874–1893. doi:10.1175/2011JPO4604.1

Zhang, W. G., D. J. McGillicuddy, and G. G. Gawarkiewicz. 2013. Is biological productivity enhanced at the New England shelfbreak front? J. Geophys. Res. Oceans **118**: 517–535. doi:10.1002/jgrc.20068

Zhang, S., C. A. Stock, E. N. Curchitser, and R. Dussin. 2019. A numerical model analysis of the mean and seasonal nitrogen budget on the Northeast U.S. Shelf. J. Geophys. Res. Oceans **124**: 2969–2991. doi:10.1029/2018JC014308

Zhang, W. (G.), and others. 2023. Cross-shelf exchange associated with a shelf-water streamer at the Mid-Atlantic Bight shelf edge. Prog. Oceanogr. **210**: 102931. doi:10.1016/j.pocean.2022.102931

Zheng, B., and others. 2023. Dinoflagellate vertical migration fuels an intense red tide. Proc. Natl. Acad. Sci. **120**: e2304590120. doi:10.1073/pnas.2304590120

19395590, 2025, 2, Downloaded from https://aslopubs.onlinelibrary.wiley.com/doi/10.1002/lno.12765 by Mbl Whoi Library, Wiley Online Library on [21/05/2025]. See the Terms and Conditions (https://onlinelibrary.wiley.com/terms-and-conditions) on Wiley Online Library for rules of use; OA articles are governed by the applicable Creative Commons License

Zheng, B., E. T. Crockford, W. Zhang, R. Ji, and H. M. Sosik. 2024. Bias-corrected high-resolution vertical nitrate profiles from the CTD rosette-mounted submersible ultraviolet nitrate analyzer. Limnol. Oceanogr. Methods. **22**: 889–902. doi:10.1002/lom3.10656

Acknowledgments

The authors acknowledge the NES-LTER team members who contributed to this work. The authors thank Kevin Cahill and Zoe Sandwith for help with analysis of the triple oxygen isotope samples and S. Alejandra Castillo Cieza, Elizabeth Lambert, Zoe Kronberg, Justin Ossiolinski, and Ellen Roosen for helping collect the O_2/Ar data. We thank Paul Henderson and WHOI nutrient analytical facility for analyzing nutrient concentrations of the discrete bottle samples. We are extremely grateful for the support of the captain, crew, and marine technicians of *R/V Endeavor*. An anonymous reviewer provided very helpful suggestions that significantly improved the quality of the manuscript. This research was supported by the National Science Foundation (OCE-1655686 and OCE-2322676) and the Simons Foundation (561126).

Conflict of Interest

None declared.

Submitted 05 June 2024
Revised 09 October 2024
Accepted 27 November 2024

Associate editor: James Leichter

19395590, 2025, 2, Downloaded from https://aslopubs.onlinelibrary.wiley.com/doi/10.1002/lno.12765 by Mbl Whoi Library, Wiley Online Library on [21/05/2025]. See the Terms and Conditions (https://onlinelibrary.wiley.com/terms-and-conditions) on Wiley Online Library for rules of use; OA articles are governed by the applicable Creative Commons License